I&EC research
Industrial & Engineering Chemistry Research



pubs.acs.org/IECR
Article

# A Cost-Efficient Electrical Impedance Tomography System for Adaptive Process Analytics

*Published as part of Industrial & Engineering Chemistry Research special issue "Smart Reactors - Towards Adaptive, Resilient, and Autonomous Process Systems".*

Tom Liebing,* Hossein Ostovar, Moritz Hollenberg, Dennis Kähler, and Thorsten A. Kern

**Cite This:** *Ind. Eng. Chem. Res.* 2026, 65, 16739–16752



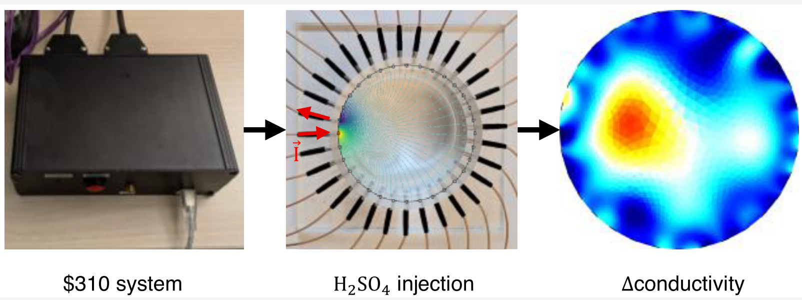


**ABSTRACT:** Electrical impedance tomography (EIT) has significant potential as a noninvasive tool for spatially resolved process monitoring, yet most reported systems remain laboratory prototypes and are rarely suitable for integration into chemical engineering environments. We present a fully embedded, low-cost EIT platform designed as a deployable tomographic sensor for in situ monitoring of reactive media in laboratory-scale reactors. The platform can be realized for approximately $442 in prototype quantities and below $310 in small-batch production. The system enables spatially resolved conductivity mapping with 32 measurement channels and is designed for straightforward integration into laboratory and reactor environments. Its compact USB-powered hardware is complemented by microcontroller firmware in C and an object-oriented Python interface for experiment control and data analysis. On-board impedance calculation allows stand-alone operation and supports real-time monitoring of dynamic conductive processes. Hardware characterization includes measurements of total harmonic distortion plus noise for signal excitation and voltage measurement with mean values up to 0.0651%, a signal frequency of 105 kHz and optimized analogue amplification across all gain settings, a variable analogue filter gain ranging from −1.35 to 34.81 dB, and characterization of the current source at excitation currents of 100 and 350 $\mu$A. Additionally, the system's performance is validated for the adjacent and opposed pair pattern, achieving a mean signal-to-noise ratio of up to 76.59 dB. The imaging performance is quantified on circular phantoms in terms of position error, spatial resolution, and detection limit, and the long-term stability is verified over a 20-h measurement with a relative drift below 0.03%. The system achieves frame rates of 7.36 to 13.18 fps depending on the measurement pattern. The system is validated in a chemically relevant scenario by monitoring the dissolution of 5 mol $L^{-1}$ $H_{2SO_{4(aq)}}$. The resulting spatial conductivity maps resolve transient concentration gradients associated with proton activity, illustrating the potential of the platform for the detection of local process states in adaptive reactor environments. Together, the characterized hardware performance and validation under chemically relevant conditions establish the platform as a scalable in situ imaging sensor suitable for integration into adaptive, data-driven reactor systems.

## ■ INTRODUCTION

Modern industrial processes in chemical engineering are complex and require advanced monitoring and control strategies to ensure optimal performance, safety, and sustainability. The precise monitoring of mixing process parameters is crucial for the optimization, efficiency, and safety of chemical processes.[1]

Conventional monitoring techniques often use point measurements, providing limited information on the overall

**Received:** March 11, 2026
**Revised:** July 17, 2026
**Accepted:** July 20, 2026
**Published:** August 2, 2026

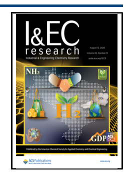






https://doi.org/10.1021/acs.iecr.6c01118
*Ind. Eng. Chem. Res.* 2026, 65, 16739–16752

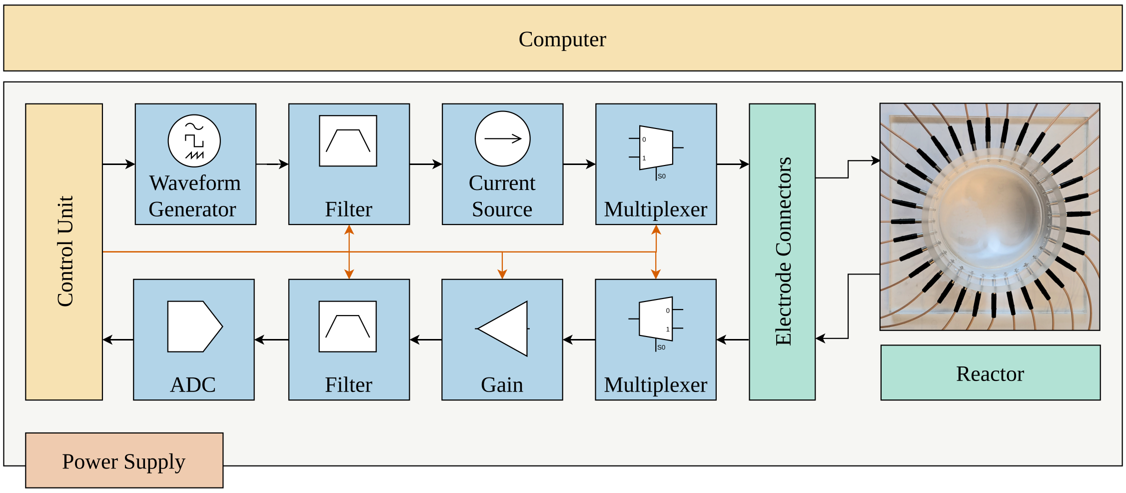


**Figure 1.** Block diagram of the functions of the EIT system. Signals are shown in black arrows, control signals in orange arrows.

process, resulting in a monitoring framework that treats the reactor as a black-box system with limited spatial observability. In contrast, spatially resolved sensing enables the detection of local process states and the detection of local inhomogeneities and gradients in mixing processes.[2−4] This high dimensional information can be leveraged for advanced control strategies to optimize the process performance. For example, poorly mixed regions can limit mass transfer and reduce effective reaction rates, whereas localized thermal hot spots may accelerate side reactions and pose safety risks to reactor operation.[5−7] The spatial information can help to precisely control the reaction and mixing conditions for ideal end product quality and resource efficiency.

Monitoring the conductivity in self-adjusting (SMART) reactors enables efficiency by dynamically adjusting to variable feedstock quality. This is particularly relevant for renewable raw materials, which often exhibit heterogeneity in composition or concentration.

Industrial processes monitoring traditionally is based on well established sensors for temperature, pressure, flow rate, and pH. These sensors provide robust and accurate measurements but are inherently point-based. Pressure sensors typically yield global values whereas temperature and velocity sensors deliver local information on fixed installed locations, such as reactor walls or preinstalled probes. Achieving detailed spatial information would require sensor arrays, which are invasive and can disturb the hydrodynamics or complicate maintenance. Parameters that exhibit strong local gradients such as temperature and pH are particularly difficult to observe with classical sensors. Local variations may occur during heating or cooling or upon injection of reactants. This can lead to local hot spots or local pH fluctuations.

Tomographic methods, in contrast, are noninvasive and enable a more detailed picture of the process state and allow advanced control strategies and monitoring. Two key technologies that overcome the limitations are distributed fiber optic sensing and process tomography. Using distributed fiber optic sensing, it is possible to measure spatial and temporal changes in temperature that remain undetected to discrete thermocouples.[8,9]

Similarly, Electrical Capacitance Tomography (ECT), Electrical Resistance Tomography (ERT) and Electrical Impedance Tomography (EIT) are noninvasive imaging techniques that provide spatially and temporal resolved information about the conductivity distribution within a process [[10], p. 10−17] [[11], p. 403−408].[12,13] Electrical Tomography is suited for any process that involves media with conductivity and/or dielectric properties.

Commercial EIT systems are mostly designed either for medical applications, such as Philips Medical pulmonary monitoring, or for specialized research setups, like Sciospec devices, and are often expensive or not optimized for rapid experimental process studies. Some devices achieve good measurement performance.[14,15] While several low-cost and portable EIT devices have been proposed,[16−18] they typically rely on external laboratory equipment, distributed system components, or lack full integration of the analog front end, digital back end, and software infrastructure.

In contrast, this work presents a fully integrated EIT system that combines signal generation, measurement front end, digital control, and host communication within a single compact enclosure. The system is designed for flexible laboratory use, with a form factor and cost optimized for rapid deployment. It is ready to use out of the box, requiring only a USB connection for power and data, and can be easily incorporated into closed-loop control systems for real-time process monitoring. Moreover, the platform is fully customizable, allowing users to adapt measurement parameters, electrode configurations, and software interfaces to suit a wide range of experimental and process-control scenarios.

The EIT measurement principle is based on electrical potentials measured at the boundary of a conductive material. These potentials are usually generated by a current with frequencies up to 1 MHz and constant amplitude. Additionally, the excitation current is selected according to the expected impedance range of the object under investigation to obtain measurable voltage levels. Two different measurement modes can be implemented, the two-terminal and four-terminal schemes. The four-terminal scheme has the benefit of eliminating the voltage drop caused by contact impedance. In this measurement scheme, the voltages at the excitation electrodes are not considered for reconstruction. The voltages measured for reconstruction, in combination with the excitation, are called the measurement pattern. The most common pattern is the adjacent pattern, where current is introduced at one electrode and leaves at the neighboring



https://doi.org/10.1021/acs.iecr.6c01118
Ind. Eng. Chem. Res. 2026, 65, 16739−16752

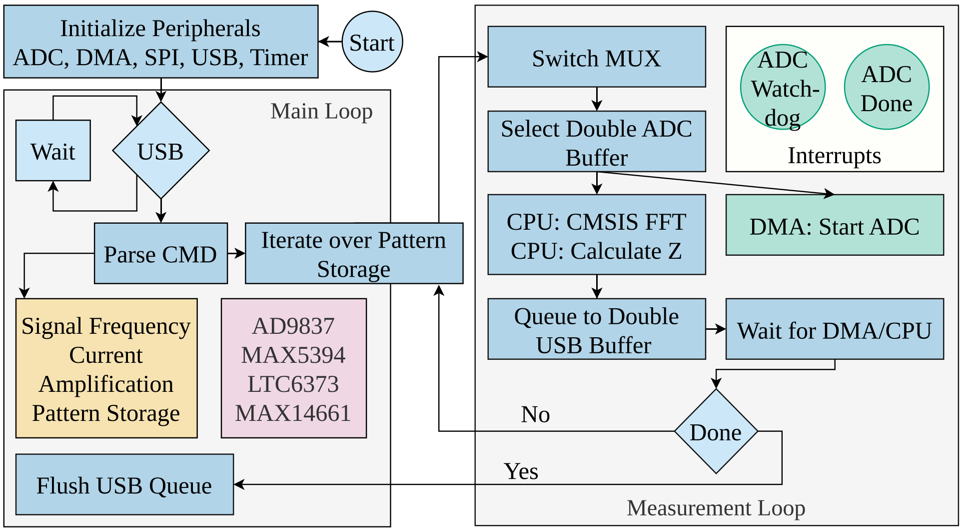


**Figure 2.** Flowchart of the MCU firmware. After initialization, the system enters the main loop where it waits for commands from the host. Upon receiving a command, it executes the corresponding function, which may involve configuring the excitation parameters, selecting electrode patterns and acquiring data. The architecture is based on direct memory access (DMA) for parallel data acquisition by the processor and acquisition by the ADC. Instead of the signal processing happening on the MCU itself, it is also possible to queue raw signal data to the USB buffer and send it.

electrode. Differential voltages are measured at all other adjacent electrodes, and this process is repeated until all electrodes have acted as exciting electrodes. In research, it is also common to use custom patterns optimized for specific use cases.[11]

Different EIT system architectures exist, ranging from multichannel parallel front ends to time-multiplexed approaches. Parallel architectures enable simultaneous voltage acquisition but significantly increase system complexity, size, and cost. Time-multiplexed systems using analog multiplexers offer greater configurational flexibility at the expense of acquisition speed.

The system described in this work is a fully integrated microcontroller (MCU) based EIT device that combines excitation, measurement, electrode multiplexing, and host communication in a single compact enclosure. Using a flexible multiplexer network, the system supports differential voltage measurements between arbitrary electrode pairs and allows single-ended current injection between any two electrodes. This design enables both two-terminal and four-terminal measurement schemes within the same hardware platform.

By enabling spatially resolved state detection in reactive media, the presented platform provides a sensing foundation for adaptive and autonomous reactor concepts envisioned in SMART process systems. Spatially resolved sensing constitutes a key prerequisite for the transition from monitored to self-adjusting reactor systems. The system is analyzed under hardware performance metrics and is validated in a chemically relevant scenario by monitoring the dissolution of 5 mol $L^{-1}$ $H_{2SO_{4(aq)}}$.

## ■ MATERIALS AND METHODS

To meet the requirements of a compact, USB-powered EIT device for lab and field applications, the system architecture was deliberately simplified. The resulting functional blocks are illustrated in Figure 1.

A microcontroller based control unit manages the integrated circuit components and coordinates excitation generation, measurement acquisition, and communication. The microcontroller configures and controls the waveform generator, the programmable current source amplitude, electrode multiplexers and demultiplexers, as well as the gain stages of the analog input filters. Furthermore, it performs analog-to-digital conversion, executes the required digital signal processing for amplitude and phase extraction, and manages bidirectional data transfer to a host computer via USB. The power supply and USB connection is galvanically isolated to reduce ground loops and minimize noise coupling. The tank used in this work consists of an acrylic cylinder serving as an electrically insulating and chemically inert housing. A total of 32 stainless steel electrodes are uniformly distributed along the inner circumference of the cylinder, forming a single measurement plane.

### Excitation Subsystem

The excitation signal is generated by an AD9837 waveform generator operating with a system clock of 16 MHz. The device can generate sinusoidal, triangular, and square waveforms. Only the sinusoidal waveform is used in this work.

The current injection stage is based on an improved Howland current source topology, providing a stable excitation current over the operating frequency range.[19]

For conditioning of the excitation signal prior to current injection, the TLV9164 operational amplifier was employed in the pre-Howland signal path. A MFB (Multiple Feedback) band-pass filter topology with order two and lowest center frequency of 105 kHz is used for DC offset removal.

In combination with the digitally controlled potentiometer (MAX5394), the center frequency and input amplitude of the current source is defined. The TLV9164 was selected due to its rail-to-rail input and output capability and sufficient gain-bandwidth product for the targeted excitation frequency, both of which are critical for accurate amplitude control and phase integrity at the input of the improved Howland current source.

To reduce system complexity and hardware overhead, the excitation current is not monitored directly. Instead, deterministic generation of amplitude and phase of the excitation current is assumed constant.

### Electrode Multiplexing

After voltage-to-current conversion, the excitation current is routed through two 16:2 multiplexers (MAX14661), which support bipolar signals. One channel of each multiplexer is used for current injection, while the second channel provides demultiplexing of the return path. The voltage signals corresponding to the selected measurement pattern are also multiplexed using two MAX14661 devices. The two




https://doi.org/10.1021/acs.iecr.6c01118
Ind. Eng. Chem. Res. 2026, 65, 16739−16752

channels on the measurement side form a differential receive pair, which is routed to the signal conditioning stage before digitization.

## Voltage Measurement Front-End

To achieve a wide range of voltage levels across different measurement patterns, the amplification range must be adjustable. Adjacent electrode configurations can result in voltage levels in the millivolt range, while custom patterns might produce significantly higher amplitudes. For flexible use in scientific setups, the signal conditioning stage should provide configurable gain. Additional requirements include DC offset removal to prevent ADC clipping, suppression of low-frequency mains interference, attenuation of high-frequency noise, antialiasing filtering and high input impedance.

In order to achieve this, a high-input-impedance instrumentation amplifier (LTC6373) with digitally configurable gain ranging from 0.25 to 16 is used to amplify the signal above the noise floor without compromising the gain−bandwidth product. A second-order differential band-pass filter is employed. It has a center frequency of 105 kHz and an additional gain of 5. To prepare the signal for digitization, a defined DC offset is added and an antialiasing filter is applied prior to the ADC.

## Digital Signal Processing and Hardware Control

The MCU STM32WB55 provides full software control, over excitation parameters and electrode selection, enabling current selection and custom voltage measurement patterns. The principle of the software flow is shown in Figure 2.

The internal ADC of the STM32WB55 supports up to 4 Msps in differential mode. The ADC and excitation frequency are chosen so that each signal period spans $N^2$ samples. The sampling rate is constrained by the CPU clock and timers, but using integer multiples of $N^2$ enables leakage-free FFT computation, allowing both the signal frequency and sample count to be selected appropriately.

A suitable combination on the STM32WB55 is

$$N = \frac{f_{\mathrm{ADC}}}{f_{\mathrm{signal}}} = \frac{3.368421\ \mathrm{MHz}}{105.263\ \mathrm{kHz}} \approx 32\ \mathrm{samples/period} \quad (1)$$

The first 64 samples are discarded to allow the analog filters to settle over two signal periods. The sampled data are then either streamed to the host PC or processed on the MCU, with a CMSIS FFT being used to compute the impedance. Raw data can also be retained on the PC for further analysis, for example, to extract additional process parameters or support research investigations.

A Python-based host interface provides object-oriented access to the data. The developed API also allows seamless integration into existing sensor networks and can be customized to accommodate specific measurement workflows or control strategies.

## Economic Viability

One scientific contribution of this work is the deterministic integration of industrial-grade analog ICs into an embedded architecture that achieves laboratory-grade signal integrity at a substantially reduced cost. As shown in Table 1, the proposed system can be realized for approximately 442 in prototype quantities and less than $ 310 in small-batch production, enabling economically viable deployment of EIT in industrial sensing applications.

## Electrical and Image Evaluation Metrics

For the evaluation of EIT systems, various phantoms can be used, such as active elements or Cole phantoms.[20−22] In this work, a resistive mesh phantom is employed to minimize system noise and provide access to multiple points for measurement and signal injection. As the focus is on analogue hardware performance rather than electrode interface modeling, neither Cole-model nor active phantoms are required. An electrical analysis of the system is performed to determine the signal-to-noise ratio (SNR), bandwidth, total harmonic distortion plus noise (THD+N), and accuracy of the system.

The system's long-term operational stability is verified on the resistive mesh phantom to determine the relative magnitude drift ensuring negligible electronic noise interference. Furthermore, the spatial fidelity of the tomographic reconstructions is characterized via a modified subset of GREIT figures of merit.[23] Specifically, Position Error (PE) and Resolution (RES) are determined for conductive and nonconductive circular phantoms. These metrics are adapted to isolate hardware-induced errors from the inherent biases of the inverse solver, providing a deterministic characterization of the system's operational precision. To statistically characterize the operational limits of the analogue front-end, $N$ = 100 frames are captured for each phantom inclusion ($d/D$ = { 6, 12, 20%}). Regularization parameters were selected independently for simulation and measurement to achieve optimal reconstruction quality for each respective noise regime. This follows standard practice in EIT, where parameters are tuned to the specific hardware and SNR conditions of each deployment. Resulting images are reported as $\mu \pm \sigma$, where the standard deviation provides a direct measure of the hardware's stochastic stability and signal-to-noise ratio. To isolate electronic errors from the algorithmic baseline of the inverse solver, three specific metrics are derived from the figures of merit. The hardware metrics Centroid Precision (CP), Spatial Fidelity (SF), and Structural Similarity (SSIM) are determined to explicitly quantify the operational agreement between physical measurements and the theoretical simulation baseline. Additionally, the injection of a 5 mol $L^{-1}$ aqueous $H_2SO_4$ solution into tap water serves as a qualitive demonstration of the system's tomographic potential in a realistic scenario.

**Table 1. System Cost Decomposition using Mouser Electronics Pricing[a]**

| category | single unit cost (USD) | batch cost (USD) |
|---|---|---|
| integrated circuits (MCU, DDS, InA, MUX) | 94.62 | 71.72 |
| passive components | 13.44 | 6.84 |
| connectors & interconnects | 8.09 | 7.32 |
| power management (isolated DC-DC, LDOs) | 12.03 | 11.10 |
| PCB manufacturing (high-TG, 4-layer) | 133.17 | 29.70 |
| enclosure (aluminum AKG 165) | 20.98 | 20.98 |
| electrode cable harness (16-Ch coaxial) | 160.00 | 160.00 |
| **total system cost** | **442.33** | **307.66** |

[a]Batch costs are calculated using the unit prices applicable for an order quantity of ten units.

## Signal-to-Noise Ratio

The frequency-domain SNR quantifies the ratio between signal power and noise power and can be used to quantify the stages and hardware characteristics [p. 2.48−2.50].[24,25] For a constant impedance, the power is proportional to the squared voltage or current, $P \propto V^2/Z$, such that the SNR for channel i is defined as

$$\mathrm{SNR}_{dB,i}^{\mathrm{FFT}} = 20\cdot\log\left(\frac{V_{\mathrm{signal},i}}{V_{\mathrm{noise},i}}\right) \quad (2)$$

where $V_{\mathrm{signal},i}$ denotes the RMS value of the signal component and $V_{\mathrm{noise},i}$ the RMS value of the noise component.

For quantification of the overall systems repeatability the time-domain SNR can be used:[26]

$$\mathrm{SNR}_{dB,i}^{\mathrm{ENS}} = 20\cdot\log\left(\frac{\mu_i}{\sigma_i}\right) \quad (3)$$

Where $\mu_i = \mathbb{E}[V_i^{\mathrm{on}}]$ is the mean value of the signal with turned on signal generation $m_i$ and the variance $\sigma_i = \sqrt{\mathrm{Var}[V_i^{\mathrm{off}}]}$ with turned off signal generation.

The overall SNR of the system is measured with the signal generation enabled and disabled using a matrix phantom as shown in Figure 3a using all resistors populated. In total 1000 frames are

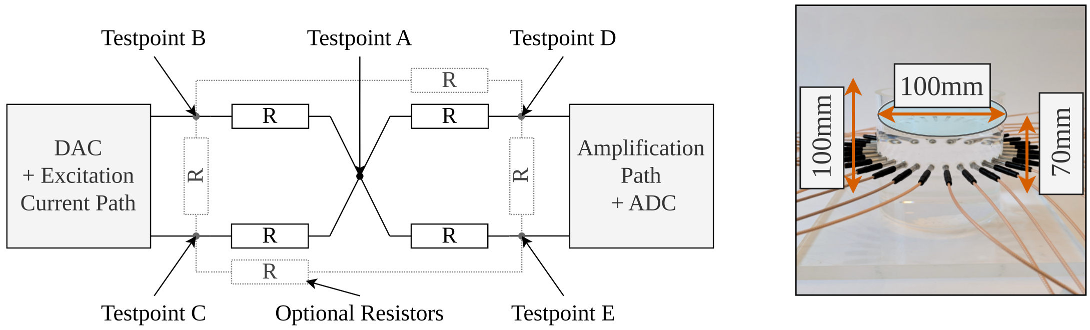


(a) Schematic of the setup to determine the evaluation metrics. Depending on populated components and chosen values, multiple setups can be built to measure different quantities.

(b) Tank dimensions and coaxial wires connected to the electrodes are shown.

**Figure 3.** Overview of the setup for evaluating the EIT system. (a) Schematic of the configurable measurement system. (b) Acrylic tank for chemically relevant testing.

recorded for each excitation position to calculate the ensemble SNR. For the FFT based SNR the standard deviation is calculated as well. The SNR is measured in a four-terminal configuration using the adjacent measurement pattern with 350 $\mu$A and a 2 k$\Omega$ configuration, showing the performance in a realistic scenario. Due to the rotational symmetry of the phantom, measurements are averaged across excitation positions such that equivalent voltage measurement pairs are combined. Specifically, the voltage measurements taken adjacent to the excitation electrodes are averaged with the corresponding neighboring voltage measurements obtained from the next excitation. A two-terminal pattern between opposite electrodes using a 100 $\mu$A current and a 10 k$\Omega$ configuration, shows the performance in an optimal case.

## Bandwidth (BW)

The BW and bode plot is an indicator on the systems stability and shows the general performance of the system in the frequency domain. The frequency response is recorded over the range from 1 kHz to 1 MHz using the Zurich Instruments MFIA Impedance Analyzer which is a high-precision lock-in-based impedance measurement system, suitable for frequency response and phase characterization.

For the current source under test a known load of 1 k$\Omega$ is used to measure the output current over frequency at a constant input amplitude. To evaluate different operating conditions two often used currents are selected, 100 and 350 $\mu$A.

The amplification path is evaluated for each gain setting of the instrumentation amplifier ranging from 0.25 to 16 using a known input signal from the MFIA.

## Total Harmonic Distortion Plus Noise (THD+*N*)

To evaluate the quality of the injected current and the measured voltage after amplification, the THD+$N$ is determined by the equation:

$$\mathrm{THD} + N = \frac{\sqrt{\sum_{k \neq k_1} |V[k]|^2}}{|V[k_1]|} \tag{4}$$

In contrast, the THD considers only the harmonic distortion components:

$$\mathrm{THD} = \frac{\sqrt{\sum_{n=2}^{H} |V[k_n]|^2}}{|V[k_1]|} \tag{5}$$

where $k$ denotes the frequency bin of the FFT, $k_1$ represents the fundamental frequency bin, and $k_n$ corresponds to the frequency bins of the $n$−th harmonic order [[25], p. 2.46−2.48].

The THD+N and THD are measured for both the current path and amplification path using the MFIA and a frequency of 105.263 kHz.

For the current path the same use cases as for the bandwidth measurement are applied using a 1 k$\Omega$ load and two different current amplitudes of 100 and 350 $\mu$A.

The amplification path is also evaluated for each gain setting as it was done for the bandwidth measurements.

## Accuracy

The full scale accuracy $A_i$ for each measurement within the pattern is calculated using the value $E[V_i]$ of the measured voltage and the normed simulated value $V_i^S$ as[26]

$$A_i = \left[1 - \frac{|E[V_i] - V_i^S|}{\max(|V^S|)}\right] \cdot 100\% \tag{6}$$

The measurements are performed using the adjacent pattern on the 2 k$\Omega$ resistive mesh phantom with 350 $\mu$A excitation current. For the adjacent pattern, the voltages are combined as described for the SNR measurement, relative to the excitation position leaving 29 measurements for one excitation. In total 1000 frames are recorded and the accuracy is calculated for each measurement point, then averaged and the standard deviation is calculated.

## Long-Term Operational Stability

Temporal robustness is validated via a 20-h continuous measurement protocol. To isolate the thermal stability of the current source and the input-referred noise of the analog circuit from the electrochemical variables of a liquid medium, measurements are performed on a 2 k$\Omega$ resistive mesh phantom. A frame is acquired every 60 s using the adjacent pattern to determine the global relative drift: $\Delta|Z|_{\mathrm{rel}}$. This drift is calculated using the following formula:

$$\Delta |Z|_{\mathrm{rel}}(t) = \frac{\sum_{i=1}^{N_M} |V_i(t) - V_i(t_0)|}{\sum_{i=1}^{N_M} |V_i(t_0)|} \cdot 100\% \tag{7}$$

where $V_i(t)$ represents the voltage of a specific measurement at time $t$. The variable $V_i(t_0)$ is the initial reference voltage, which is is averaged over the first 10 measurements. Finally, $N_M$ stands for the total number of measurements within a single frame.

To quantify temporal signal stability, a channel-wise coefficient of variation (CV) is defined for each of the $N_M$ = 928 voltage measurements within a frame. For every measurement channel $i$, corresponds to a unique current-injection and voltage-pickup electrode combination. The temporal mean $\mu_{V,i}$ and standard deviation $\sigma_{V,i}$ are computed across all acquired frames. The CV is then defined as


https://doi.org/10.1021/acs.iecr.6c01118
Ind. Eng. Chem. Res. 2026, 65, 16739−16752

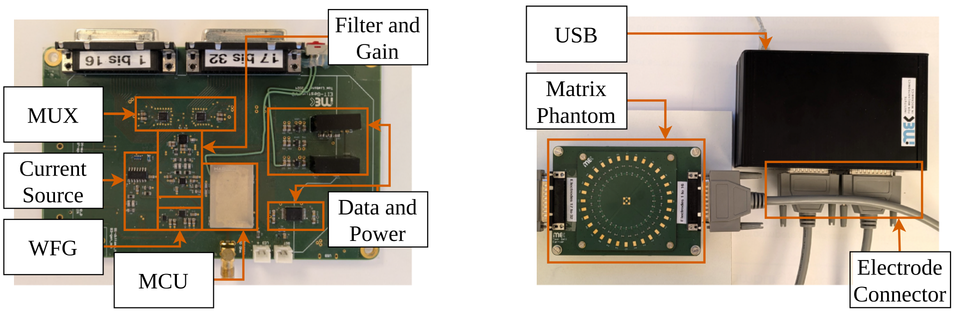


(a) Internal PCB, designed for this work. (b) System in a box and 2 kΩ resistive mesh phantom.

**Figure 4.** Detailled system overview. (a) Internal PCB view. (b) Encased system in a box and 2 kΩ resistive mesh phantom.

$$CV_i = \frac{\sigma_{V,i}}{\mu_{V,i}} \cdot 100\% \tag{8}$$

providing a per-channel measure of temporal repeatability independent of absolute signal magnitude.

### Centroid Precision

To quantify positional accuracy, the positional error (PE) is determined for each frame. Let $\hat{\mathbf{x}}_q$ be the binary set of pixels exceeding a 75% amplitude threshold, to ensure robustness against reconstruction artifacts. To suppress ghost artifacts, the CoG is computed exclusively from the largest connected component. The reconstructed centroid $\mathbf{r}_q$ is calculated as the first spatial moment of this set:

$$\mathbf{r}_q = \frac{1}{N_q} \sum_{i \in \hat{\mathbf{x}}_q} \mathbf{r}_i \tag{9}$$

where $\mathbf{r}_i$ denotes the normalized coordinates of the $i$th pixel and $N_q$ is the pixel count. The PE is defined as the Euclidean distance $\|\mathbf{r}_q - \mathbf{r}_t\|$between the reconstructed and true phantom coordinates $\mathbf{r}_t$, expressed as a percentage of the tank radius.[23,27] The CP is then partitioned to isolate hardware-induced shift:

$$\mathrm{CP} = \left[1 - \frac{|\mathrm{PE}_{\mathrm{meas}} - \mathrm{PE}_{\mathrm{sim}}|}{100}\right] \cdot 100\% \tag{10}$$

### Spatial Fidelity

The spatial spread of the reconstructed inclusion is characterized by the resolution, defined as the radius ratio:

$$\mathrm{RES} = \sqrt{\frac{A_q}{A_0}} \tag{11}$$

where $A_q$ is the area of the thresholded set $\hat{\mathbf{x}}_q$ and $A_0$ is the total area of the sensing domain.[23] To evaluate the efficiency of the analog front-end in preserving theoretical sharpness, the SF is calculated as the ratio of simulated to experimental resolution ($\mathrm{RES}_{\mathrm{sim}}/\mathrm{RES}_{\mathrm{meas}}$). A fidelity of 100% indicates that the hardware operates at the theoretical limit of the inverse solver.

### Structural Similarity

To assess global morphological preservation between the mean experimental frame and the noise-free simulation, the SSIM is employed.[28] Both images are normalized to [0, 1] and compared via:

$$\mathrm{SSIM}(\hat{\mathbf{x}}_{\mathrm{meas}}, \hat{\mathbf{x}}_{\mathrm{sim}}) = \frac{(2\mu_m\mu_s + c_1)(2\sigma_{ms} + c_2)}{(\mu_m^2 + \mu_s^2 + c_1)(\sigma_m^2 + \sigma_s^2 + c_2)} \tag{12}$$

where $\mu$ and $\sigma$ denote local means and standard deviations of the normalized conductivity maps, and $c_1$, $c_2$ are numerical stabilization constants, derived from the dynamic range of the pixel values.[28] Additionally, the Pearson correlation $r$ between the two images is computed over all pixels within the sensing domain as a complementary linear similarity measure.

### Temporal Performance

To assess the temporal performance of the system using the 928-measurement adjacent-electrode pattern the hardware frame rate is determined.

The effective system frame rate represents the usable repetition rate achieved by the host PC, incorporating the hardware acquisition and the subsequent data transmission overhead. This is calculated by measuring the elapsed clock time on the host from the transmission of the measurement command to the reception of the final data byte, averaged over 100 consecutive frames.

### Monitoring of the Dissolution of Sulfuric Acid

The dissolution of sulfuric acid in water represents an exothermic process accompanied by a rapid increase in ionic concentration and electrical conductivity. Due to the dissociation of $H_2SO_4$ in aqueous solution, spatial gradients in temperature and conductivity can occur during the mixing process, particularly in the initial phase before complete homogenization.[29,30]

The solution was not mechanically stirred and the mixing proceeded by diffusion and free convection only. The unstirred condition was chosen to create a localized, reproducible conductivity perturbation, allowing the spatial and temporal resolution of the system to be demonstrated. The experiment was performed at room temperature. We report a single representative dissolution run, as the temporal repeatability of the measurement hardware is independently characterized using both the resistive mesh and phantoms.

To evaluate the capability of the proposed EIT system for monitoring conductivity distributions, 100 $\mu$L of 5 mol $L^{-1}$ $H_2SO_{4(aq)}$ was injected into the tank filled with 550 mL tap water. The tap water's conductivity was measured to be 504 $\mu$S $cm^{-1}$.

EIT measurements were acquired continuously during the dissolution and mixing process using the adjacent stimulation pattern described above.

The spatial conductivity reconstruction allows visualization of the temporal evolution of the dissolution process, including the formation and subsequent dispersion of highly conductive regions. This experiment demonstrates the suitability of the system for monitoring chemically relevant mixing and reaction phenomena in conductive process media.

## ■ RESULTS AND DISCUSSION

The realized hardware platform is shown in Figure 4. The resulting device is a compact, USB-powered EIT system with galvanically isolated power and data paths, effectively preventing ground loops and minimizing measurement noise. Currently implemented is data transmission via virtual COM port, but other faster protocols can be implemented. With the printed circuit board (PCB) already providing a dedicated layout for a WiFi antenna, in further versions, the system can be extended toward distributed deployment within industrial process environments. Figure 4b shows the system encased in an aluminum box with the 2 kΩ resistive mesh phantom. The




https://doi.org/10.1021/acs.iecr.6c01118
Ind. Eng. Chem. Res. 2026, 65, 16739−16752

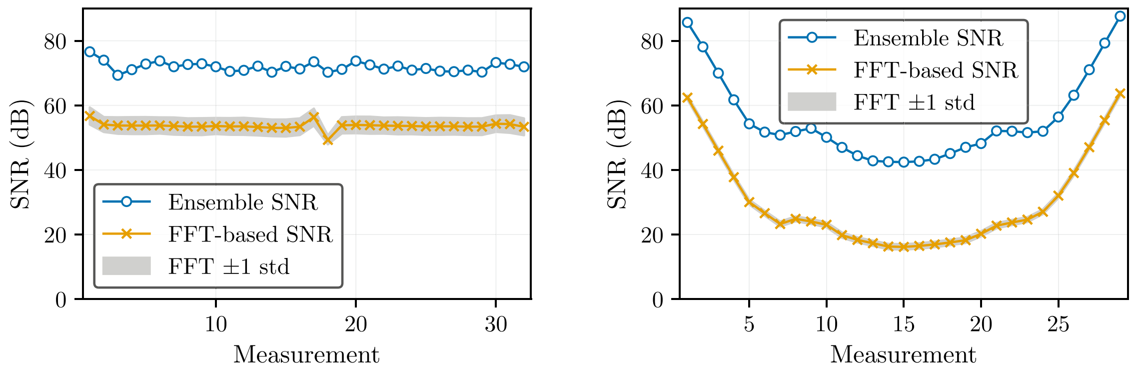


(a) Opposed electrode configuration (b) Adjacent measurement pattern

**Figure 5.** Pattern-averaged FFT SNR is compared to the ensemble SNR at the excitation frequency, highlighting the difference between total electronic noise and measurement repeatability using the 10 kΩ matrix phantom. (a) Signal and noise are recorded in a two terminal measurement between the opposite electrodes using the optimal operating conditions. (b) The signal is recorded in a four terminal measurement using the adjacent pattern.

encased box proviedes shielding and a robust housing. Figure 4a shows the internal PCB. Visible are the main components as well as the electrode connectors on the top side of the PCB. Also visible is a later added switch to select the boot mode of the MCU, which is not part of the original design.

## Signal-to-Noise Ratio

The plots in Figure 5 show the mean SNR and the standard deviation across the 1000 measurements. Figure 5a shows the SNR for the two-terminal measurement between opposite electrodes, while Figure 5b shows the SNR for the adjacent measurement pattern. In the two-terminal opposite-electrode configuration, the current path and voltage sensing geometry are identical for all channels, leading to signal amplitudes and noise levels that are nearly uniform. Consequently, the SNR is predicted to remain constant across channels, with any deviations primarily from instrumentation noise, gain tolerances, and residual channel-to-channel mismatches.

Since the contact impedance in the resistive mesh phantom is negligible, compared to the overall impedance and the typical real world process media, the SNR is close to the ideal SNR of the system.

The small standard deviation of the SNR across repeated measurements indicates optimal temporal stability of the measurement system. However, for the adjacent measurement pattern, the measured voltage depends on the relative position of the electrode pair with respect to the current injection electrodes. Channels in close proximity to the current injection exhibit higher signal amplitudes and, consequently, higher SNR, than channels at greater distance to the excitation electrodes.

The ensemble SNR is systematically higher than the broadband FFT-based SNR because it only considers fluctuations of the signal at the excitation frequency across repeated measurements. Consequently, the ensemble SNR primarily reflects measurement repeatability and short-term system stability at the driven frequency. In contrast, the broadband FFT-based SNR includes contributions from electronic noise over the entire frequency spectrum. The difference between the two SNR metrics therefore quantifies the influence of broadband noise on the measurement and provides an estimate of the effective noise contribution outside the excitation frequency.

Table 2 shows the SNR statistics for the two-terminal measurement between opposite electrodes and the adjacent measurement pattern, respectively. For the two terminal measurement, the mean and standard deviation across all measurements are calculated and in ideal case all channels should have the same SNR, while for the adjacent pattern only the minimum and maximum values are shown as the SNR varies across the channels.

**Table 2. SNR Statistics for Ensemble and FFT-Based SNR for Two-Terminal Measurements[a]**

| SNR (dB) | mean | std | min | max |
|---|---|---|---|---|
| opposed ensemble | 71.91 | 1.45 | 69.32 | 76.59 |
| opposed FFT-based | 53.65 | 1.09 | 49.30 | 56.70 |
| adjacent ensemble | | | 42.42 | 87.62 |
| adjacent FFT-based | | | 16.17 | 63.68 |

[a]For the opposed electrode configuration, all channels exhibit identical SNR in the ideal case. Mean, standard deviation, minimum, and maximum values across channels are shown. For the adjacent configuration, the SNR varies per channel and only minimum and maximum values are shown.

## Bandwidth

Figure 6 shows the bandwidth measurement of both the current path and amplification path. The center frequency of the amplification path is 105 kHz for all gain settings as shown in Figure 6a. It shows excellent agreement with the designed center frequency and the capability of removing the DC offset within two periods of the signal. This allows an effective trade off between settling time and temporal resolution. Additional the bandpass filter suppresses higher frequency noise. The frequency response of the current path also shows the desired behavior. The input filter of the current controlling voltage removes the DC component and high frequency sampling noise prior to the current source as shown in Figure 6b. The settling frequency depends on the selected input amplitude and center frequency.

The current path is shown for two typical operating currents of 100 and 350 $\mu$A. The input filter of the current source removes the DC component to ensure a bipolar signal around 0 V, which prevents electrode polarization and enables


https://doi.org/10.1021/acs.iecr.6c01118
Ind. Eng. Chem. Res. 2026, 65, 16739−16752

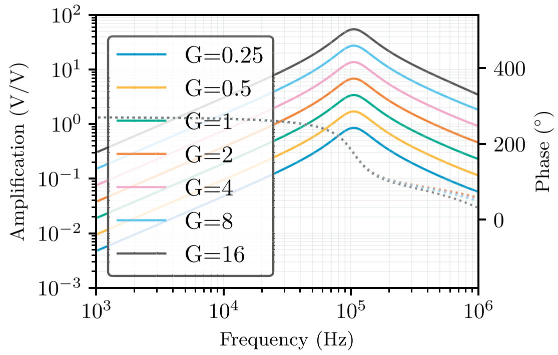


(a) Transfer function of the amplification path.

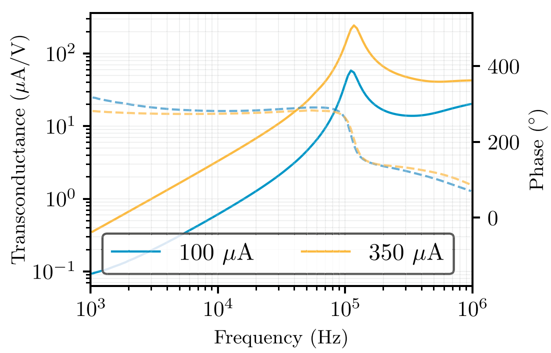


(b) Transfer function of the current path

**Figure 6.** Plot (a) shows the transfer functions of the amplification path and its different gain settings. (b) shows the transfer function of the current path for two different operating currents.

accurate impedance measurements under realistic process conditions.

## Total Harmonic Distortion Plus Noise

Table 3 shows the summary of the distortion measurements for the current source and amplification path.

**Table 3. Statistical Summary of Distortion Measurements for the Current Source and Amplification Path**[a]

| metric | mean (%) | std (%) | min (%) | max (%) |
|---|---|---|---|---|
| | | Current Source | | |
| THD | 0.4897 | 0.3436 | 0.1503 | 1.0585 |
| THD+N | 0.7738 | 0.3482 | 0.3401 | 1.1334 |
| | | Amplification Path | | |
| THD | 0.0083 | 0.0051 | 0.0039 | 0.0197 |
| THD+N | 0.0651 | 0.0642 | 0.0159 | 0.2095 |

[a]Measuremtents are performed at 105.263 kHz and for the loads of 1 and 10 kΩ at two different currents of 100 and 350 μA. The amplification path is evaluated for each gain setting as it was done for the bandwidth measurements.

The THD of the current source shows good linearity, but still contains a noise floor dominating the overal distortion. The higher THD+N value indicates a broadband noise which can be reduced using averaging techniques, distortion components however cannot be reduced this way.

In contrast the amplification path shows a significantly lower distortion. It shows excellent linearity and a low noise floor and will not limit the performance of the system.

The THD can be improved in further iterations of the design by using higher linearity components and improving the measurement setup to reduce external interference.

## Accuracy

The accuracy of the system for the adjacent pattern is shown in Figure 7. The overall mean accuray for all the channels is 98.41% with a standard deviation of 0.72%. The maximum accuracy is 99.61%. On channel one a low accuracy of 86.09% is observed. No corresponding irregularities were identified in the data processing code, suggesting that the reduced accuracy is likely caused by nonideal hardware effects in the measurement chain.

Figure 7 also shows the standard deviation of the measurements across the 1000 measurements. The standard deviation is higher for the channels with lower SNR and for those who are further away from the excitation electrodes, which is expected as the signal amplitude is lower and the noise has a higher impact on the measurement.

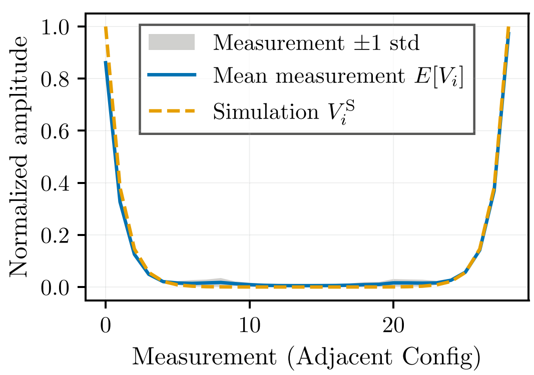


(a) Simulated vs. measured voltage amplitudes.

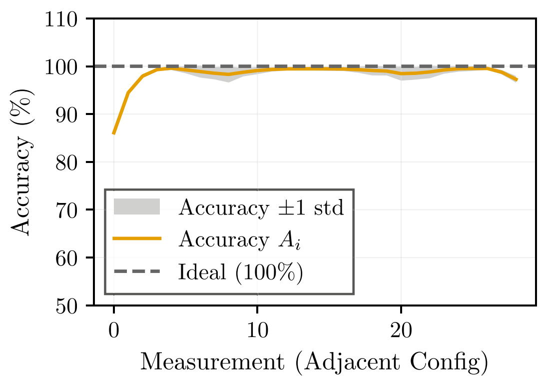


(b) Accuracy of the adjacent measurement pattern.

**Figure 7.** Accuracy of the overall system using the adjacent pattern on the 2 kΩ resistive mesh phantom with 350 μA excitation current. (a) displays the agreement between measured and simulated voltage amplitudes. (b) shows the accuracy $A_i$ for each measurement point, demonstrating the system's performance across the dynamic range.


https://doi.org/10.1021/acs.iecr.6c01118
Ind. Eng. Chem. Res. 2026, 65, 16739−16752

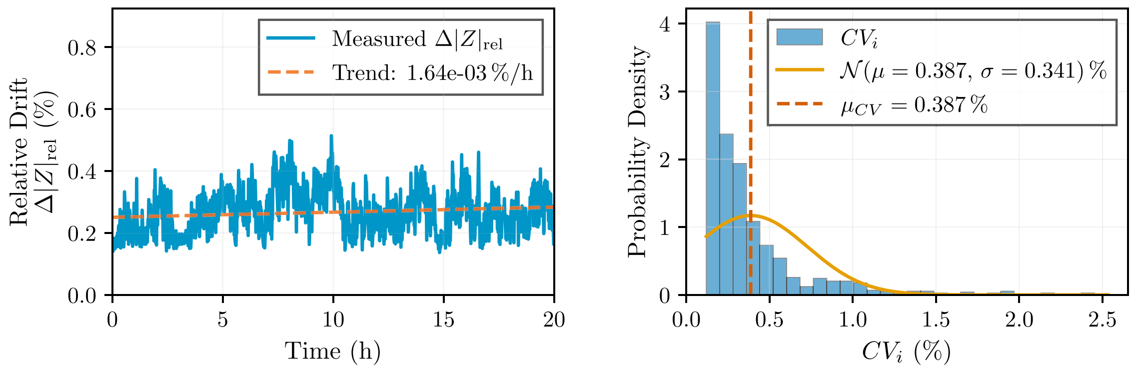


(a) Temporal drift of the system.

(b) Coefficient of variation of the system.

**Figure 8.** Long-term operational stability over 20 h on a resistive mesh phantom. One frame per 60 s is captured at 200 $\mu$A and an INA gain of 4. (a) Global relative drift $\Delta|Z|_{\text{rel}}$ as a function of time, exhibiting near-linear evolution with a slope of $1.64 \times 10^{-3}$%/h and a total accumulated drift below 0.03%. (b) Distribution of the per-channel coefficient of variation $CV_i$ across all individual measurements within a frame; mean $\mu_{CV} \approx$ 0.387%.

**Table 4. Imaging Metrics Grouped by Phantom Diameter and Position, Averaged over Conductive and Insulating Rod Types[a]**

| | | PE (% $r_{\text{tank}}$) | | RES | | |
|---|---|---|---|---|---|---|
| diameter | position | sim | meas | sim | meas | *r* |
| 20 mm | center | 1.94 | 2.5 ± 0.1 | 0.246 | 0.265 ± 0.058 | 0.867 |
| | eccentric | 1.55 | 10.7 ± 6.3 | 0.188 | 0.195 ± 0.015 | 0.593 |
| 10 mm | center | 1.72 | 2.4 ± 0.0 | 0.264 | 0.326 ± 0.027 | 0.840 |
| | eccentric | 1.13 | 4.1 ± 1.1 | 0.164 | 0.180 ± 0.022 | 0.735 |
| 6 mm† | center | 1.94 | 13.9 ± 15.1 | 0.255 | 0.349 ± 0.097 | 0.703 |
| | eccentric | 0.74 | 8.9 ± 1.2 | 0.168 | 0.236 ± 0.054 | 0.606 |

[a]PE: position error (% of tank radius $r_{\text{tank}}$ = 50 mm). *RES*: normalised resolution radius. *r*: Pearson correlation between mean measurement frame and noise-free simulation. Measurement values: mean ± standard deviation over 100 frames, averaged over conductor and insulator variants. Dagger (†): configuration at or below the practical detection limit.

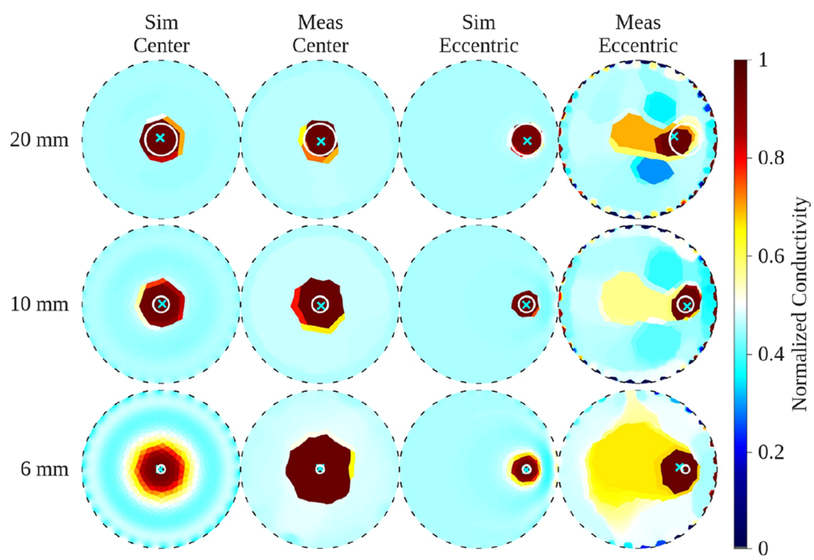


**Figure 9.** Reconstruction comparison for conductive cylindrical phantoms of three diameters (6, 10, 20 mm) at tank center and radially eccentric position (30 mm, 60% of tank radius). Rows alternate between noise-free simulation and a representative frame of $N$ = 100 consecutive hardware measurements. Reconstructions were obtained with the EIDORS toolbox[32,33] using a TV-PDIPM solver ($\lambda = 5 \times 10^{-5}$, 10 iterations). The white circle indicates the true phantom boundary.

## Long-Term Operational Stability

The EIT system demonstrated high long-term stability over the 20-h measurement window ($N_M$ = 928 channels, one frame per 60 s). The global relative drift $\Delta|Z|_{\text{rel}}$ evolved near-linearly with a slope of $1.64 \times 10^{-3}$%/h, corresponding to a total accumulated drift below 0.03% over the full observation period shown in Figure 8a. The mean coefficient of variation across all measurement channels was $\mu_{CV} \approx$ 0.387%, confirming that temporal signal variation per channel is negligible relative to the signal magnitude (Figure 8b).



https://doi.org/10.1021/acs.iecr.6c01118
Ind. Eng. Chem. Res. 2026, 65, 16739−16752

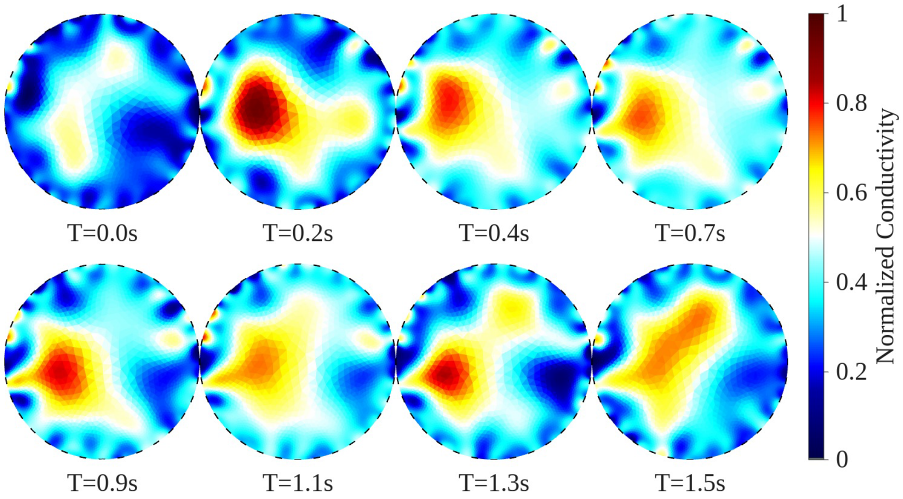


(a) Sequence of eight conductivity reconstructions acquired within 1.5 s. The images were reconstructed using the EIDORS toolbox [32, 33] with a Gauss-Newton solver and a Gaussian hyperparameter prior ($\lambda = 0.01$).

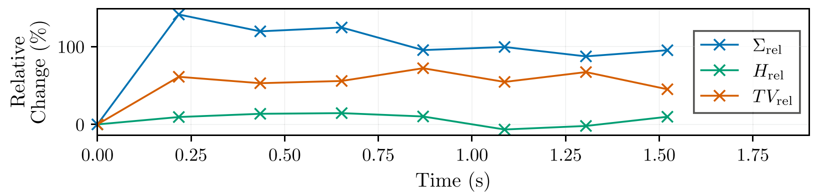


(b) Integrated conductivity $\Sigma_{\mathrm{rel}} = \Delta\int_{\Omega} \sigma \, \mathrm{d}A \, / \, |\Sigma_0|$; spatial heterogeneity index $H_{\mathrm{rel}} = \Delta H \, / \, |H_0|$ (coefficient of variation of $|\sigma|$); total variation $\mathrm{TV}_{\mathrm{rel}} = \Delta\mathrm{TV} \, / \, |\mathrm{TV}_0|$ summed over interior mesh edges.

**Figure 10.** Reconstruction of 5 mol $L^{-1}$ $H_{2SO_{4(aq)}}$ injected into a water-filled tank. (a) Time sequence of reconstructed conductivity distributions. (b) Three quantitative process indicators extracted from the FEM conductivity field, quantifying the total conductivity increase, spatial heterogeneity, and local conductivity gradients during the dissolution process.

These results confirm that neither the current source nor the analog front-end introduces measurable systematic drift within the observation window, validating the system's suitability for continuous long-term monitoring applications. Power-line interference is suppressed by design at several stages. The system is USB-powered with no direct mains connection, and both power and data paths are galvanically isolated, breaking ground loops and removing any earth-referenced path through which 50/60 Hz could couple into the analog front-end. Excitation and detection operate at 105 kHz, more than 3 orders of magnitude above the mains frequency, placing the line and its low-order harmonics deep in the stopband of the second-order differential band-pass front-end. Because the impedance is computed from a single leakage-free FFT bin at the excitation frequency, residual mains components fall in unused bins and do not enter the reconstruction. Consistent with this, the 20 h measurement shows drift below 0.03% and a low broadband noise floor, indicating effective rejection of mains pickup.

## Temporal Performance

The achievable frame rate of the EIT system is determined by three interdependent factors: the choice of measurement pattern, the per-measurement acquisition and processing duration, and the total number of measurements per frame. These factors represent a fundamental trade-off between spatial reconstruction accuracy, which benefits from a larger, more diverse measurement set, and temporal resolution. Determining the optimal operating point for a given process or experimental application is beyond the scope of this study. The results characterize the achievable limits for two representative patterns.

For the common adjacent-drive adjacent-measurement pattern with 32 electrodes (928 measurements per frame), a mean frame rate of 7.36 kHz (135.9 ms, $\sigma$ = 0.5 ms) was measured over 100 consecutive acquisitions. For the opposed pattern (16 opposite excitation pairs, 448 measurements per frame), a mean frame rate of 13.18 kHz (75.9 ms, $\sigma$ = 0.4 ms) was achieved. The low standard deviation in both cases confirms deterministic timing governed by hardware ADC sampling, with negligible host-side jitter.

## Position Error

Table 4 summarizes PE and RES for all 12 configurations, comparing the single noise-free simulation reconstruction against the per-frame measurement statistics (Figure 9).

For large phantoms at the tank center (20 mm and 10 mm), the measured PE closely tracks the simulation floor, with discrepancies below 1% of the tank radius and near-zero frame-to-frame standard deviation ($\sigma_{\mathrm{PE}} \leq 0.1\%$). This indicates that positional accuracy is limited by the inverse solver, not the analog front-end. For eccentric phantoms, the measured PE rises well above the simulation floor, reaching $\mathrm{PE}_{\mathrm{meas}}$ = 10. Seven % for the 20 mm eccentric configuration, shown in


https://doi.org/10.1021/acs.iecr.6c01118
Ind. Eng. Chem. Res. 2026, 65, 16739−16752

Table 4, consistent with the known radial dependence of position error in linear EIT reconstruction.[23]

The 6 mm phantoms exhibit substantially elevated PE and frame-to-frame variability ($\sigma_{PE}$ up to 15.1%, 6 mm center), indicating that this size approaches the practical detection limit of the system at the given tank geometry. The 6 mm configurations yield $PE_{meas}$ = 13. Nine % at the center and 8.9% eccentric, shown in Table 4, confirming that sub-10 mm inclusions cannot be localized reliably under hardware conditions.

## Spatial Resolution

The RES metric, representing the normalized radius of the thresholded reconstruction, remains low across all configurations ($\sigma_{RES} \leq 0.097$), with the largest frame-to-frame spread for the 6 mm center phantom, confirming the hardware's temporal consistency in spatial spread. For 20 mm and 10 mm center phantoms, measured RES agrees with simulation to within ΔRES < 0.08. The 6 mm conductive center phantom yields the largest deviation ($RES_{meas} = 0.417$ vs $RES_{sim} = 0.270$, conductive variant), consistent with the known oversmearing of spatially under-resolved inclusions by TV-regularized solvers.[31]

## Image Fidelity

SSIM and Pearson correlation $r$ between the mean measurement frame and the noise-free simulation were computed over all pixels within the sensing domain. Combined results are shown in Table 4.

Center phantoms of 10 and 20 mm diameter yield $r \geq 0.84$, with the conductive variants reaching $r = 0.90$−$0.92$. Eccentric configurations show lower correlation $r \geq 0.593$, attributable to the positional shift observed in PE. Across all 12 configurations, the mean Pearson correlation is $\overline{r} = 0.73$, and the mean SSIM is 0.826, indicating globally moderate-to-good structural preservation of the theoretical reconstruction.

## Hardware Error Partitioning

To isolate the contribution of the hardware to the total reconstruction error, the CP and spatial fidelity SF were computed. Averaged over all 12 phantom configurations, $P_{pos}$ = 94. Eight % and $F_{res}$ = 99. Four %, with a mean hardware-induced position bias of ΔPE = 5.22% and resolution dilution of ΔRES = 0.031. The near-unity spatial fidelity confirms that the hardware does not introduce additional image blurring beyond what the inverse solver produces on noise-free simulation data. The residual position bias is concentrated in the eccentric and small-diameter configurations, where reconstruction sensitivity is reduced.

## Reconstruction of the Dissolution of Sulfuric Acid

The spatial reconstruction of the dissolution process is shown in Figure 10a. A drop of conductivity change is observed in the second image on the left side of the tank indicating a strong gradient of ionic concentration.

The reconstruction is performed as time-difference EIT, with each frame referenced to the initial state. To provide quantitative process indicators independent of absolute conductivity values, three scalar metrics are extracted from the reconstructed FEM conductivity field at each time step, shown in Figure 10b. The integrated relative conductivity change $\Sigma_{rel}$, a spatial heterogeneity index $H_{rel}$ defined as the coefficient of variation of the conductivity across the domain, and the total variation $TV_{rel}$ summed over the interior mesh edges are extracted. The integrated conductivity $\Sigma_{rel}$ is the most robust indicator. It rises sharply to approximately 140% in the first frame after injection and then settles toward 100%, tracking the bulk increase in ionic concentration and its subsequent redistribution.

This reflects the substantial increase in ionic concentration caused by the 100 $\mu$Ldrop of 5 mol $L^{-1}$ $H_2SO_4$ in 550 mL of water yielding a proton concentration of roughly 1.8 mmol/L, which corresponds to an estimated physical increase of about 126%.

The heterogeneity and total-variation indices both rise immediately after injection and remain nonzero and fluctuating throughout the observation window, without converging back to the baseline. This indicates that pronounced local conductivity gradients persist and that the medium does not fully homogenize within the 1.5 s interval, consistent with the localized structure still visible in the final reconstructed frames of Figure 10a. The heterogeneity index $H_{rel}$ is more sensitive to reconstruction noise than $\Sigma_{rel}$ and is interpreted only at the level of its overall trend. All three are relative, normalized descriptors of the reconstructed field and characterize the temporal evolution of the process rather than absolute physical values.

The reconstructed images reflect the relative changes in a trend rather than absolute physical conditions, due to the difference solver and the regularized inversion. Nevertheless, the observed increase and subsequent stabilization of the integrated conductivity capture the underlying mixing dynamics. For control purposes, the regulation would rely on a consistent sensor response rather than in absolute parameter accuracy. An absolute quantification would require additional calibration.

The reconstructed conductivity reflects the total ionic conductivity of the medium, which depends on both ion concentration and temperature. A single-frequency EIT measurement therefore cannot, on its own, separate concentration-induced from temperature-induced conductivity changes. In the dissolution experiment this ambiguity is not significant. The injected $H_2SO_4$ releases on the order of tens of joules of dilution enthalpy, corresponding to a bulk temperature rise below 0.1 °C and a temperature-induced conductivity change of well under 1%, negligible against the ~140% change driven by the concentration increase.[34] The observed signal is thus dominated by ionic concentration.

For general process conditions where thermal gradients are non-negligible, disambiguation requires either model-based correction or data fusion with independent point temperature sensors, which are already standard in industrial reactors and can be integrated through the system's Python host interface, combining the spatially resolved EIT field with localized thermal references. Absolute quantification at each position would additionally require local calibration against known reference conductivities to map boundary measurements to absolute voxel conductivity. Separating these physical contributions is beyond the scope of the present hardware-focused study and is identified as a direction for future work.

## System Limitations

Several factors define the operating envelope of the present system. The system images media that are at least weakly ionically conductive, and the reactive fluid must provide a measurable conductivity in the region and at the stage of the process of interest. Purely nonconductive media such as gases or nonpolar liquids are therefore not suitable as the continuous




https://doi.org/10.1021/acs.iecr.6c01118
Ind. Eng. Chem. Res. 2026, 65, 16739−16752

**Table 5. Comparison of EIT Hardware Systems**

| system/work | type | electrodes | frequency range | frame rate |
|---|---|---|---|---|
| PulmoVista 500[35] | Comm. Med. | 16 | 80 kHz−130 kHz | 50 fps |
| Maltron Sheffield MK 3.5[36] | Comm. Med. | 8 | 2 kHz−1.62 MHz | 25 fps |
| Sciospec EIT32/64/128+[38] | Comm./Sci. | up to 256 | 100 kHz−1 MHz | 100 fps |
| Dickin and Wang[14] | Sci. Ind. (ERT) | 16−64 | 75 kHz−163.6 kHz | 20 fps |
| Khalighi et al.[17] | Sci. Ind. | 32 | 10 kHz−250 kHz | |
| Król et al.[13] | Sci. | 32 | 1 kHz | 10 to 15 fps |
| KIT4[18] | Sci. | 16 inj. 80 meas. | 1 kHz−120 kHz | 31.25 fps |
| **this work** | Sci. Ind. | 32 | opt. for 100 kHz | 7.36 fps/13.18 fps |

phase. Nonconductive phases dispersed within a conductive medium, such as gas bubbles or immiscible droplets, can in principle be imaged as conductivity contrasts, provided their dynamics are slow relative to the acquisition frame rate characterized in the temporal performance evaluation.

The achievable spatial resolution is governed by the electrode spacing relative to the domain size rather than by the absolute vessel diameter. The size-dependent behavior is reflected in the phantom evaluation, where the smallest inclusions approach the detection limit, while larger vessels can be accommodated by increasing the electrode count or by accepting a proportionally coarser resolution, supported by the software-configurable electrode and pattern settings.

The present implementation assumes an electrically insulating vessel wall. A conductive, for example metallic, wall introduces a parasitic low-resistance path that is expected to degrade the measurement, although a sufficiently large electrode-to-wall distance may keep this path negligible. A detailed study of this case is left for future work.

The concentration−temperature ambiguity and the calibration required for absolute quantification are discussed in the dissolution section. The dissolution experiment itself is intended as a demonstration of the system's imaging capability and was not cross-validated against an independent chemical reference such as multipoint conductivity probes or titration sampling. As a first-order chemical consistency check, the measured integrated conductivity increase (peaking near 140%) agrees in magnitude with the ≈126% increase predicted independently from the known injected dose, the residual difference being consistent with the transient peak and regularization. The quantitative imaging performance of the hardware is instead established independently through the phantom study, and absolute chemical quantification is identified as a direction for future work.

The stainless steel electrodes used here are suitable for short-term measurements, while long-term exposure to strongly corrosive media has not been evaluated. Because the system operates in a four-terminal scheme, the measurement is insensitive to contact impedance at the electrode interface, so interface degradation has limited impact on the reconstruction. Physical corrosion of the electrode material itself remains a separate concern, and as the electrode material is interchangeable, chemically resistant alternatives such as graphite or noble-metal-coated electrodes can be substituted for aggressive media. Operation was characterized at room temperature, and performance under elevated process temperatures, which primarily affects the analog components, has not been evaluated. Both aspects are left for future work.

## Performance Benchmarking

Table 5 shows representative EIT and ERT platforms spanning commercial medical devices, commercial scientific instruments, and academic research systems, providing context for the design choices of the present work. The commercial medical systems[35,36] are engineered to strict regulatory standards and achieve reliable frame rates suitable for clinical monitoring. However, both are restricted to a fixed electrode count optimized for pulmonary or gastric applications, offer no configurability of the measurement protocol, and have high prices.[35,3735,37]

[38]Reference 38 represents the high end of commercially available scientific instruments, offering a broad frequency range, up to 256 electrode channels, and a high frame rate at the cost of a modular benchtop form factor and a correspondingly high instrument price. While its flexibility is well suited to research settings with access to dedicated laboratory infrastructure, deployment in compact or field-portable reactor environments is not its design intent.

Among academic systems,[14] is an early and foundational contribution to hardware design for industrial electrical resistance tomography. The work addresses multielectrode impedance measurement across a wide frequency range but is not a deployable integrated platform.[17] present a low-cost 32-electrode design with a wide operating frequency range and explicit attention to cost reduction. However, the system relies on distributed components and no frame rate is reported, limiting direct performance comparison.[13] demonstrate a 32-electrode system applied to fermentation process control, but the hardware is a commercially purchased Netrix unit with no disclosed price, and the reported frame rate of 10 to 15 fps reflects the combined latency of data acquisition and GPU-accelerated neural network inference rather than a hardware acquisition rate. The KIT4 system[18] achieves a robust frame rate and multifrequency capability, but is assembled from National Instruments PXI rack modules and a custom add-on unit housed across three transport cases.

The present work addresses the gap between these categories. Unlike the commercial medical devices, it is not application-locked. The measurement pattern, excitation frequency, and amplification gain are fully software-configurable at runtime. In contrast to the academic systems surveyed, all functional blocks, waveform synthesis, current injection, electrode multiplexing, signal conditioning, on-board impedance computation, and host communication, are integrated within a single enclosed PCB, enabling stand-alone operation. This level of hardware integration is not demonstrated by any of the compared systems. At 32 channels and a frame rate of 7.36 fps, for the adjacent pattern, to 13.18 fps for the opposed pattern, the system delivers spatially resolved measurements at rates compatible with the slow dynamics of chemical reactor processes, at a fraction of the cost of existing solutions. Furthermore, the active electrode count is freely configurable in software, reducing from 32 to 16




https://doi.org/10.1021/acs.iecr.6c01118
Ind. Eng. Chem. Res. 2026, 65, 16739−16752

electrodes decreases the number of adjacent-pattern measurements per frame, yielding an approximately 4.5-fold increase in frame rate

## CONCLUSION

The presented EIT system is compact and integrated within a single enclosure, featuring dedicated control and evaluation software. Within this constrained form factor and cost, the achieved performance is well aligned with the intended application scope.

The evaluation establishes the system's imaging performance on circular phantoms, with reliable localization down to 10 mm inclusions and 6 mm at the detection limit, and confirms long-term stability with a drift below 0.03% over 20 h. The system reaches 7.36 fps (adjacent) to 13.18 fps (opposed), and this level of integration is achieved at a low component cost as shown in Table 1, positioning it as a deployable alternative to laboratory and commercial EIT systems.

The higher and more uniform SNR observed for the opposed electrode configuration is consistent with the symmetric current paths and identical channel sensitivities expected in this measurement geometry. In contrast, the commonly used four-terminal adjacent pattern exhibits the expected channel-dependent variations.

The distortion analysis reveals that the current source is the dominant nonideality in the analogue signal chain. Despite the identified noise contributions in the current source, the system performance is excellent for its low cost and compact design. In contrast, the amplification path exhibits substantially lower THD and THD+N values, confirming that it does not limit system performance under the investigated conditions. Improving the current source design and board layout would be most promising for further enhancing system performance in future iterations. Such improvements are expected to increase SNR, particularly for the adjacent measurement pattern, while reduced distortion would further improve the accuracy of voltage extraction. A firmware update can increase the acquisition rate and the capability to monitor rapid changes in conductive process media.

Although only the standard adjacent and opposed stimulation patterns were used in this study, the system allows for custom patterns, which could enable targeted measurements in reactors and improve feedback control.

In the envisioned closed-loop use, scalar indicators extracted from the reconstruction, such as the integrated conductivity change and the spatial heterogeneity index introduced here, serve as the controlled variable. A detected mixing deficiency or local concentration deviation can then be acted upon through standard reactor actuators, for example by adjusting stirrer speed, feed or dosing rate, injection location, or recirculation flow, after which the effect is reimaged to close the loop. The present work provides the spatially resolved sensing and the quantitative indicators required for such control, while demonstrating the control loop itself is beyond the scope of this study.

The EIT reconstructions of the $H_2SO_4$ dissolution capture the rapid local increase in conductivity near the injection point. While the absolute amplitudes are attenuated by regularization and model limitations, the relative trends accurately reflect the temporal evolution of the process and are sufficient to guide monitoring and feedback control.

## ASSOCIATED CONTENT

### Data Availability Statement

The hardware and software implementation as well as hardware measurements corresponding to the results presented in this paper is available via the institutional repository TORE.[39]

## AUTHOR INFORMATION


### Corresponding Author

**Tom Liebing** − *Institute for Mechatronics in Mechanics, Hamburg University of Technology, 21073 Hamburg, Germany;* orcid.org/0000-0003-3162-4783; Email: tom.liebing@tuhh.de

### Authors

**Hossein Ostovar** − *Institute of Chemical Reaction Engineering, Hamburg University of Technology, 21073 Hamburg, Germany;* orcid.org/0000-0001-9371-1589

**Moritz Hollenberg** − *Institute for Mechatronics in Mechanics, Hamburg University of Technology, 21073 Hamburg, Germany*

**Dennis Kähler** − *Institute for Mechatronics in Mechanics, Hamburg University of Technology, 21073 Hamburg, Germany*

**Thorsten A. Kern** − *Institute for Mechatronics in Mechanics, Hamburg University of Technology, 21073 Hamburg, Germany; United Nations University Hub on Engineering to Face Climate Change at the Hamburg University of Technology, United Nations University Institute for Water, Environment and Health, 21073 Hamburg, Germany*

Complete contact information is available at: https://pubs.acs.org/10.1021/acs.iecr.6c01118


### Notes

The authors declare no competing financial interest.

## ACKNOWLEDGMENTS

The authors gratefully acknowledge the collaborative research program SMART Reactors, funded by the Deutsche Forschungsgemeinschaft, Germany (DFG, German Research Foundation; SFB 1615 503850735), for making this work possible.

## REFERENCES


(1) Bowler, A. L.; Bakalis, S.; Watson, N. J. A Review of In-Line and on-Line Measurement Techniques to Monitor Industrial Mixing Processes. *Chem. Eng. Res. Des.* **2020**, *153*, 463−495.

(2) Abdul Wahab, Y.; Abdul Rahim, R.; Fazalul Rahiman, M. H.; Ridzuan Aw, S.; Mohd Yunus, F. R.; Goh, C. L.; Abdul Rahim, H.; Ling, L. P. Non-Invasive Process Tomography in Chemical Mixtures - A Review. *Sens. Actuators, B* **2015**, *210*, 602−617.

(3) Stehle, M.; Sheppard, T. L.; Thomann, M.; Fischer, A.; Besser, H.; Pfleging, W.; Grunwaldt, J.-D. Spatial Activity Profiling along a Fixed Bed of Powder Catalyst during Selective Oxidation of Propylene to Acrolein. *Catal. Sci. Technol.* **2021**, *11*, 5781−5790.

(4) Fitschen, J.; Hofmann, S.; Wutz, J.; Kameke, A.; Hoffmann, M.; Wucherpfennig, T.; Schlüter, M. Novel Evaluation Method to Determine the Local Mixing Time Distribution in Stirred Tank Reactors. *Chem. Eng. Sci.:X* **2021**, *10*, No. 100098.

(5) Curl, R. L. Dispersed Phase Mixing: I. Theory and Effects in Simple Reactors. *AIChE J.* **1963**, *9*, 175−181.

(6) Danckwerts, P. The effect of incomplete mixing on homogeneous reactions. *Chem. Eng. Sci.* **1958**, *8*, 93−102.

(7) Moilanen, P.; Laakkonen, M.; Visuri, O.; Aittamaa, J. Modeling Local Gas-Liquid Mass Transfer in Agitated Viscous Shear-Thinning Dispersions with CFD. *Ind. Eng. Chem. Res.* **2007**, *46*, 7289−7299.
(8) Sahota, J. K.; Gupta, N.; Dhawan, D. Fiber Bragg Grating Sensors for Monitoring of Physical Parameters: A Comprehensive Review. *Opt. Eng.* **2020**, *59*, No. 060901.
(9) Dutz, F. J.; Heinrich, A.; Bank, R.; Koch, A. W.; Roths, J. Fiber-Optic Multipoint Sensor System with Low Drift for the Long-Term Monitoring of High-Temperature Distributions in Chemical Reactors. *Sensors* **2019**, *19*, 5476.
(10) *Electrical Capacitance Tomography*, 2nd ed.; Wang, M., Ed., Woodhead Publishing Series in Electronic and Optical Materials; Woodhead Publishing: Cambridge, 2022. ISBN: 978-0-12-823015-2.
(11) Adler, A.; Holder, D. *Electrical Impedance Tomography: Methods, History and Applications*, 2nd ed.CRC Press: Boca Raton, 2021; ISBN: 978−0-429−39988−6 DOI: 10.1201/9780429399886.
(12) York, T. Status of Electrical Tomography in Industrial Applications. *J. Electron. Imaging* **2001**, *10*, 608.
(13) Król, K.; Kłosowski, G.; Rymarczyk, T.; Gauda, K.; Kulisz, M.; Golec, E.; Surowiec, A. Process Control via Electrical Impedance Tomography for Energy-Aware Industrial Systems. *Energies* **2025**, *18*, 5956.
(14) Dickin, F.; Wang, M. Electrical Resistance Tomography for Process Applications. *Meas. Sci. Technol.* **1996**, *7*, 247−260.
(15) Dong, F.; Xu, C.; Zhang, Z.; Ren, S. Design of Parallel Electrical Resistance Tomography System for Measuring Multiphase Flow. *Chin. J. Chem. Eng.* **2012**, *20*, 368−379.
(16) Zamora-Arellano, F.; López-Bonilla, O. R.; García-Guerrero, E. E.; Olguín-Tiznado, J. E.; Inzunza-González, E.; López-Mancilla, D.; Tlelo-Cuautle, E. Development of a Portable, Reliable and Low-Cost Electrical Impedance Tomography System Using an Embedded System. *Electronics* **2021**, *10*, 15.
(17) Khalighi, M.; Vosoughi Vahdat, B.; Mortazavi, M.; Hy, W.; Soleimani, M.Practical Design of Low-Cost Instrumentation for Industrial Electrical Impedance Tomography (EIT). In *2012 IEEE International Instrumentation and Measurement Technology Conference Proceedings* 2012; pp 1259−1263 .
(18) Kourunen, J.; Savolainen, T.; Lehikoinen, A.; Vauhkonen, M.; Heikkinen, L. M. Suitability of a PXI Platform for an Electrical Impedance Tomography System. *Meas. Sci. Technol.* **2009**, *20*, No. 015503.
(19) Vazquez Lam, I. *Analysis of Improved Howland Current Pump Configurations; Application Report SBOA437A Texas Instruments*, **2020**.
(20) Schneider, I. D.; Kleffel, R.; Jennings, D.; Courtenay, A. J. Design of an Electrical Impedance Tomography Phantom Using Active Elements. *Med. Biol. Eng. Comput.* **2000**, *38*, 390−394.
(21) Griffiths, H. A Phantom for Electrical Impedance Tomography. *Clin. Phys. Physiol. Meas.* **1988**, *9*, 15−20.
(22) Griffiths, H. A. Cole Phantom for EIT. *Physiol. Meas.* **1995**, *16*, A29−A38.
(23) Adler, A.; Arnold, J. H.; Bayford, R.; et al. GREIT: A Unified Approach to 2D Linear EIT Reconstruction of Lung Images. *Physiol. Meas.* **2009**, *30*, S35−S55.
(24) IEEE-SA *IEEE Standard for Terminology and Test Methods for Analog-to-Digital Converters*; IEEE Instrumentation & Measurement Society: New York, NY, USA, 2011, ISBN: 978−0-7381−6239−3.
(25) Kester, W.-n. C. *Analog-Digital Conversion*; Analog Devices: USA, 2004 ISBN: 978−0-916550−27−1.
(26) Gagnon, H.; Cousineau, M.; Adler, A.; Hartinger, A. E. A Resistive Mesh Phantom for Assessing the Performance of EIT Systems. *IEEE Trans. Biomed. Eng.* **2010**, *57*, 2257−2266.
(27) Adler, A.; Guardo, R. Electrical Impedance Tomography: Regularized Imaging and Contrast Detection. *IEEE Trans. Med. Imaging* **1996**, *15*, 170−179.
(28) Wang, Z.; Bovik; Sheikh, A.; Simoncelli, H.; Image, E. Quality Assessment: From Error Visibility to Structural Similarity. *IEEE Trans. Image Process.* **2004**, *13*, 600−612.
(29) Leaist, D. G. Diffusion in Aqueous Solutions of Sulfuric Acid. *Can. J. Chem.* **1984**, *62*, 1692−1697.
(30) Edward, J. T.; Wang, I. C. Ultraviolet Study of the Ionization of Bisulfate Ion. *Can. J. Chem.* **1965**, *43*, 2867−2871.
(31) Borsic, A.; Graham, B.; Adler, A.; Lionheart, W. In Vivo Impedance Imaging With Total Variation Regularization. *IEEE Trans. Med. Imaging* **2010**, *29*, 44−54.
(32) Adler, A.; Lionheart, W. R. B. Uses and Abuses of EIDORS: An Extensible Software Base for EIT. *Physiol. Meas.* **2006**, *27*, S25−S42.
(33) EIDORS: Electrical Impedance Tomography and Diffuse Optical Tomography Reconstruction Software. https://eidors3d.sourceforge.net/ (accessed June 15, 2026).
(34) Bhuiyan, M. I. H.; Mavinic, D. S.; Beckie, R. D. Determination of Temperature Dependence of Electrical Conductivity and Its Relationship with Ionic Strength of Anaerobic Digester Supernatant, for Struvite Formation. *J. Environ. Eng.* **2009**, *135*, 1221−1226.
(35) Drägerwerk AG & Co. KGaA Dräger PulmoVista 500 ICU Ventilation and Respiratory Monitoring. https://www.draeger.com/Content/Documents/Products/pulmovista-500-sw1-30-pi-9109716-en-master.pdf (accessed June 15, 2026).
(36) Maltron Sheffield MK 3.5. https://maltronint.com/electrical-impedance-tomography/ (accessed June 15, 2026).
(37) NICE *PulmoVista 500 for Monitoring Ventilation in Critical Care*; National Institute for Health and Care Excellence: UK, 2019, ISBN: 978−1-4731−3622−9.
(38) Sciospec EIT32/64/128+, https://sciospec.com/product/eit32-64-128/ (accessed June 15, 2026).
(39) Liebing, T.; Kern, T. A. *A Cost-Efficient, USB Powered and Pattern Flexible Electrical Impedance Tomography System* DOI: 10.15480/882.16788.